nature physics

ARTICLES

https://doi.org/10.1038/s41567-020-0898-5

# Interference of chiral Andreev edge states

Lingfei Zhao[1]✉, Ethan G. Arnault[1], Alexey Bondarev[1], Andrew Seredinski[1], Trevyn F. Q. Larson[1], Anne W. Draelos[1], Hengming Li[2], Kenji Watanabe[3], Takashi Taniguchi[3], François Amet[2], Harold U. Baranger[1] and Gleb Finkelstein[1]✉

**The search for topological excitations such as Majorana fermions has spurred interest in the boundaries between distinct quantum states. Here, we explore an interface between two prototypical phases of electrons with conceptually different ground states: the integer quantum Hall insulator and the *s*-wave superconductor. We find clear signatures of hybridized electron and hole states similar to chiral Majorana fermions, which we refer to as chiral Andreev edge states (CAESs). These propagate along the interface in the direction determined by the magnetic field and their interference can turn an incoming electron into an outgoing electron or hole, depending on the phase accumulated by the CAESs along their path. Our results demonstrate that these excitations can propagate and interfere over a significant length, opening future possibilities for their coherent manipulation.**

The superconducting proximity effect describes the processes in which correlations are induced in a normal metal by a superconducting electrode[1]. The microscopic origin of the proximity effect lies in the Andreev reflections that couple the electron and hole states at the border of a normal metal and a superconductor. In the past few years, interest in Andreev processes has experienced a renaissance, driven by the promise of producing exotic states and excitations, such as Majorana zero modes and chiral Majorana fermions[2], which may be used for topological quantum computing[3,4]. Many concrete implementations of Majorana modes have been proposed, relying on superconductors proximitizing materials with spin–orbit coupling[5] or various quantum Hall systems[6,7].

In this work, we directly probe chiral Andreev edge states (CAESs), which result from inducing superconducting correlations in the integer quantum Hall edge states. Semiclassically, CAESs result from skipping orbit trajectories, in which an electron turns into a hole and back into an electron upon successive Andreev reflections from a superconductor. Quantum mechanically, this combination of Andreev reflections and quantum Hall edge states yields fermionic modes in which the electron and hole states are hybridized and propagate chirally along the quantum Hall–superconductor interface[8–10]. Under certain conditions, CAESs are predicted to be self-conjugate, becoming chiral Majorana fermions[11–14].

The early search for CAESs in III–V semiconductor devices focused on magneto-conductance oscillations in the quantum Hall regime[15,16]. Later, graphene samples in the quantum Hall regime were shown to have enhanced conductance between superconducting contacts[17,18]. Recent progress in making transparent type II superconducting contacts to both GaAs[19] and encapsulated graphene[20,21] has enabled the observation of several new phenomena, including edge-state-mediated supercurrent[22,23], crossed Andreev conversion[24] and inter-Landau-level Andreev reflection[25].

Nevertheless, despite some recent attempts[26–28], direct evidence for CAESs remains elusive. To conclusively identify CAESs one must demonstrate their propagation along the superconducting contact. Naively, one may expect that any electrical signal spreading along the contact will be shunted by the superconductor. Here, we demonstrate that this is not the case. The main mechanism allowing us to detect CAESs in this work is their interference, which can be described as follows: an incoming electron approaching the superconducting contact is decomposed into a linear combination of CAESs[10] propagating along the quantum Hall–superconductor interface with different wavevectors. The accumulated phase difference between these modes can result in the original electron turning into a hole as it exits the opposite end of the interface[29,30]. The appearance of the hole can then be detected by measuring the voltage on a normal contact located downstream from the grounded superconducting contact[24]. We observe a beating signal, which proves that the CAESs are formed by a coherent superposition of the electron and hole amplitudes. By further analysing the interference between the CAESs, we show that these modes are, on average, neutral—their electron and hole components have roughly equal weight. These results demonstrate that transport measurements can detect the presence of CAESs despite their charge neutrality. Our approach opens the door for detecting chiral Majorana modes in topological superconductors.

## CAES interference

Our samples are made from graphene encapsulated in hexagonal boron nitride (hBN). The graphene-hBN heterostructure is deposited on a doped Si wafer capped with a 280 nm $SiO_2$ layer, which serves as a back gate. One-dimensional contacts are made to the heterostructure[31] using both normal and superconducting metal electrodes, as shown in Fig. 1a. The superconducting electrodes are composed of a sputtered molybdenum-rhenium alloy (MoRe), a type II superconductor with an upper critical field $H_{c2} \approx 10$ T, a critical temperature of $T_c \approx 10$ K and a superconducting gap of $\Delta_0 \approx 1.3$ meV. We have previously demonstrated that the interface between MoRe and graphene is highly transparent[32], as further confirmed in Supplementary Fig. 3. In addition to the superconducting electrodes, the sample has several normal contacts made of thermally evaporated Cr/Au.

The lengths of the top and bottom graphene–superconductor interfaces, $L$, are 150 nm and 600 nm, respectively. We focus on the bottom contact ('c' in Fig. 1a). The $L = 600$ nm length is chosen so that it falls in the range between the induced superconducting

---

[1]Department of Physics, Duke University, Durham, NC, USA. [2]Department of Physics and Astronomy, Appalachian State University, Boone, NC, USA. [3]Advanced Materials Laboratory, NIMS, Tsukuba, Japan. ✉e-mail: lz117@duke.edu; gleb@phy.duke.edu

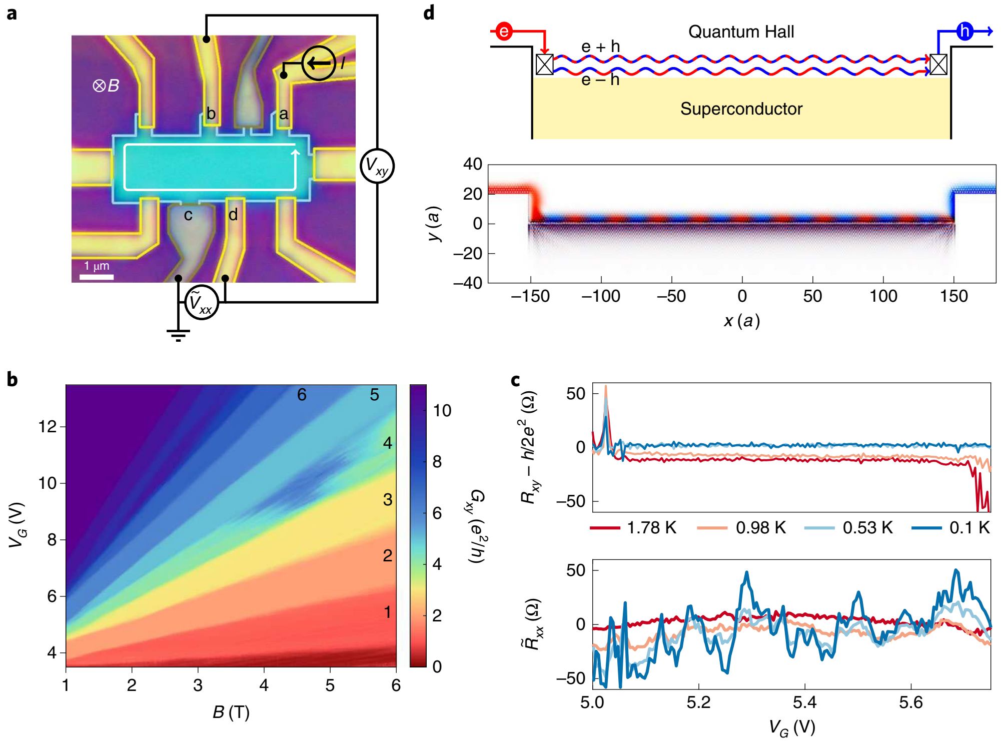

**Fig. 1 | Andreev reflection in the quantum Hall regime. a**, An optical image of the sample. Superconducting contacts (grey) are placed between normal contacts (gold). A magnetic field is applied into the plane, resulting in counterclockwise travel of electrons and holes when the graphene (blue) is n-doped. We use a four-terminal scheme to measure the Hall voltage $V_{xy}$ simultaneously with the superconductor downstream longitudinal voltage $\tilde{V}_{xx}$. The sign of $\tilde{V}_{xx}$ is carefully defined as the voltage of contact 'd' minus the voltage at contact 'c'. **b**, Fan diagram of the zero-bias Hall conductance $G_{xy}$. Filling factors are labelled on the plateaux. Degeneracy of the Landau levels starts to lift around $B=1$ T, suggesting the high quality of the graphene region. **c**, Temperature dependence of the zero-bias superconductor downstream longitudinal resistance $\tilde{R}_{xx}$ measured for $\nu=2$ at $B=3$ T (bottom) and the simultaneously measured Hall resistance $R_{xy}$ (top). To highlight the Hall quantization, $h/2e^2$ is subtracted from $R_{xy}$. The oscillations of $\tilde{R}_{xx}$ on the $\nu=2$ plateau disappear at 1.8 K. **d**, At a certain gate voltage $V_G$, an electron injected into a pair of CAESs exits as a hole. The bottom panel shows the electron (red) and hole (blue) wavefunction densities from a tight-binding calculation in the lowest Landau level. Here, the unit $a$ is the lattice parameter of graphene.

coherence length, $\xi_s = \hbar v/\pi\Delta_0 \approx 160$ nm, and the phase coherence length of quantum Hall edge states, $\xi_\varphi = \hbar v/2\pi k_B T$ (ref. [33]), which is about 12 µm at $T=0.1$ K. In this estimate, the velocity of the edge states, $v$, is taken to be equal to the Fermi velocity of graphene, $v_F = 1\times10^6$ m s$^{-1}$. Although this is typically true only for sharp vacuum edges[34], our simulation (Supplementary Section 6) suggests that the CAES velocity is probably lower but comparable to $v_F$, which places $L=600$ nm comfortably between $\xi_\varphi$ and $\xi_s$. This condition ensures both that the propagation of the CAES along the contact is quantum-mechanically coherent and that the crossed Andreev conversion[24] is suppressed.

Throughout these measurements, we apply a current from the normal contact labelled 'a' while keeping the bottom superconducting contact 'c' grounded (Fig. 1a). The current is comprised of a variable d.c. component, $I$, and a small a.c. excitation of 10 nA that allows us to measure the differential resistance. To probe CAES propagation along the superconducting contact, we study the longitudinal resistance, $\tilde{R}_{xx} = d\tilde{V}_{xx}/dI$, where $\tilde{V}_{xx}$ is measured between the normal contact 'd' and the adjacent grounded superconducting contact 'c'. We refer to this quantity as the 'downstream resistance' to reflect the quantum Hall intuition that the edge states propagate along the chiral direction and thus contact 'd' is located downstream from contact 'c'. In conventional devices with normal contacts, $\tilde{R}_{xx}$ would correspond to the longitudinal resistance $R_{xx}$, which is zero on quantum Hall plateaux and positive between them (Supplementary Fig. 1).

We also simultaneously measure the differential Hall conductance, $G_{xy} = dI/dV_{xy}$, where the transverse voltage is measured between the normal contacts 'b' and 'd' in Fig. 1a. This quantity remains well quantized through the relevant range of gate voltages and at temperatures below 3 K. This ensures that the bulk of the sample is gapped and that transport occurs only through the edge states. In the data presented, the sample is held at the base temperature below 100 mK, unless otherwise specified, and the MoRe remains superconducting at all magnetic fields ($B<6$ T) and temperatures studied.

Figure 1b presents a map of Hall conductance $G_{xy}$ measured versus $B$ and gate voltage $V_G$. The valley and spin degeneracies in this sample start to lift at $B\approx1$ T, leading to the appearance of all integer filling factors, $\nu$. The broken symmetry states have smaller activation gaps than the main sequence of filling factors $\nu=4(n+1/2)$. To ensure that the bulk of the sample remains insulating when we vary the current bias and temperature, we focus on the robust filling factor $\nu=2$ (filled lowest Landau level), which has an energy gap on the order of tens of meV. Figure 1c plots the simultaneous measurement of $\tilde{R}_{xx}$ and $R_{xy}$ versus $V_G$ in the range corresponding to the Landau level filling factor $\nu=2$ at $B=3$ T. We subtract $h/2e^2$ from $R_{xy}$ to highlight the degree of Hall quantization on the same scale as the variations of $\tilde{R}_{xx}$. Clearly, the Hall conductance is well quantized, despite the fact that the current flows through a superconducting drain contact. (Deviations of the plateau level from the quantized value for the individual curves are probably caused by the slow drift of our home-made amplifier.) The observed quantization is in agreement with the Landauer–Büttiker formula described in Supplementary Section 3, which shows that $R_{xy}$ measured between

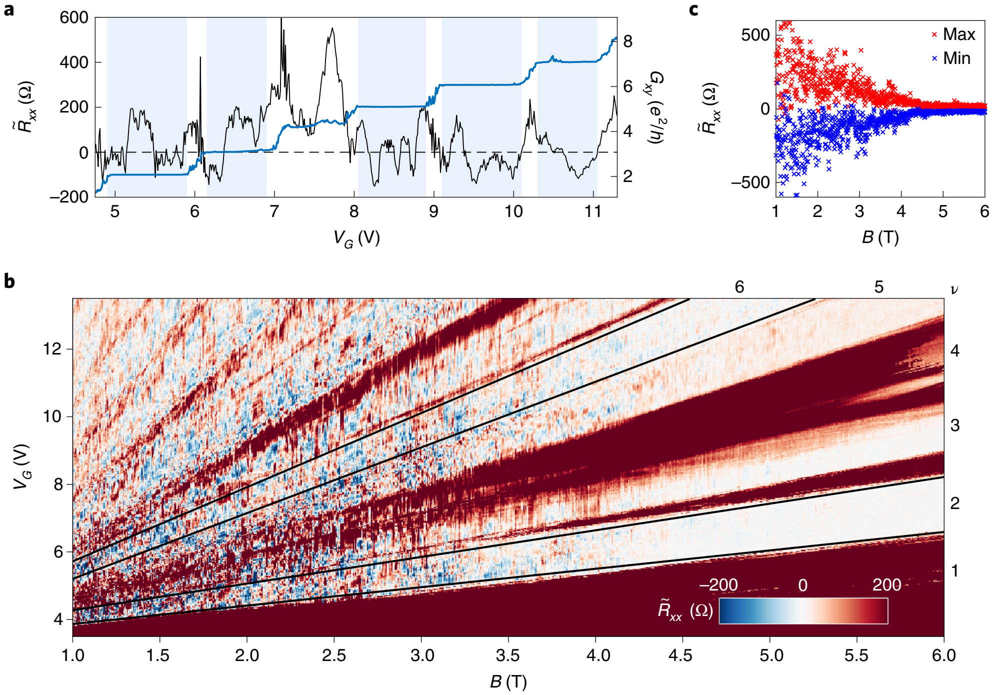

**Fig. 2 | The interference of CAESs on various quantum Hall plateaus and its magnetic field dependence. a**, Zero-bias $\tilde{R}_{xx}$ plotted versus gate voltage $V_G$ at $B=3$ T together with the simultaneously measured $G_{xy}$. $\tilde{R}_{xx}$ oscillates around zero on the well quantized plateaus of $\nu=2$, 3, 5, 6 and 7 (shaded regions). **b**, Zero-bias $\tilde{R}_{xx}$ plotted versus gate voltage $V_G$ and magnetic field $B$. Filling factors are labelled based on the $G_{xy}$ fan diagram in Fig. 1b, with the boundaries for $\nu=2$ and 6 drawn as black lines. The oscillations in the well-quantized region gradually die out with increasing magnetic field. **c**, Peak values of $\tilde{R}_{xx}$. The maximum and minimum of $\tilde{R}_{xx}(V_G)$ on the $\nu=2$ plateau are plotted versus $B$. On average, $\tilde{R}_{xx}$ varies around zero, indicating that the CAESs are roughly equal superpositions of electrons and holes.

the normal contacts 'b' and 'd' should be quantized, regardless of the properties of the drain contact.

We focus next on the range of gate voltages ($5\,\text{V} < V_G < 5.7\,\text{V}$) in which $R_{xy}$ remains well quantized at $h/2e^2$, even at higher temperature ($T < 3$ K), ruling out any possible contribution from the bulk. Remarkably, in this range, the downstream resistance $\tilde{R}_{xx}$ shows clear deviations from the zero signal usually expected in the quantum Hall regime (Supplementary Section 1). As the temperature is increased, $\tilde{R}_{xx}$ gradually flattens and approaches zero, and eventually a conventional quantum Hall behaviour of zero longitudinal resistance is recovered around 2 K. Note that this temperature is still very small compared to the quantum Hall gap and indeed $G_{xy}$ remains well quantized. We further verified that a non-zero $\tilde{R}_{xx}$ signal is observed only when the grounded contact is superconducting; the resistance measured downstream from a normal contact is strictly zero (Supplementary Figs. 1 and 2). We conclude that the deviation of $\tilde{R}_{xx}$ from zero observed for grounded contact 'c' is due to superconductivity, the influence of which is suppressed by raising the temperature. Incidentally, the vanishing of $\tilde{R}_{xx}$ observed around 2 K suggests that contact 'c' would be fully transparent in its normal state (see Supplementary Fig. 3 for a discussion of contact transparency in terms of Blonder–Tinkham–Klapwijk theory).

Notably, $\tilde{R}_{xx}$ becomes negative at some gate voltages, suggesting that contact 'd' acquires a chemical potential lower than the chemical potential of the grounded contact 'c'. We attribute this behaviour to the following process: an electron approaching the superconductor turns into a linear combination of CAESs. For each electron state, a pair of CAESs is formed when the proximity effect couples the electron edge state with the hole edge state at the same energy[10] (Supplementary Sections 2 and 6). Because their wavevectors are different, the two CAESs acquire a phase difference while propagating along the superconducting interface, resulting in a beating pattern between the electron and hole components of the wavefunction[30]. If the CAES interference produces a hole at the end of the graphene–superconductor interface, the hole will flow to contact 'd' and lower its chemical potential. Note that, in contrast to ref. [24], which studies crossed Andreev conversion across the superconductor, the negative signal observed here is due to the interference of CAES propagating along the contact. As a result, $\tilde{R}_{xx}$ is sensitive to the phase accumulated along the interface, which makes it dependent on the gate voltage.

In the following, we support our interpretation by conducting tight-binding simulations that illustrate how the CAESs propagate along the superconducting contacts, resulting in oscillations of the electron and hole probability along the interface. We then provide further experimental evidence that confirms this picture by showing that the downstream signal is sensitive to the configuration of vortices in the superconducting contacts, and that the measured fluctuations average to zero when sampled over a wide range of magnetic fields.

## Tight-binding simulations

We conducted detailed tight-binding calculations for a quantum Hall–superconductor interface (Supplementary Section 6). The superconducting contacts are modelled by a square lattice; this breaks the valley symmetry at the interface, which would otherwise determine the result of the Andreev reflections through valley isospin conservation[35]. We expect the square lattice to provide a generic representation of the rough graphene–MoRe interface. Qualitatively similar results were obtained for a superconductor modelled by a disordered honeycomb lattice.

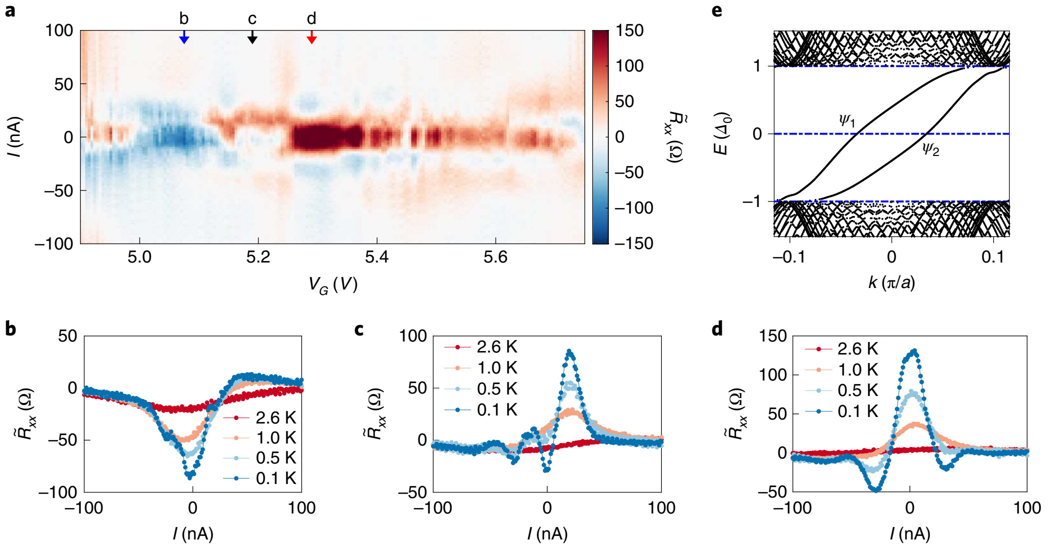

**Fig. 3 | The bias dependence of the interference effect. a**, The superconductor downstream longitudinal resistance $\tilde{R}_{xx}$ plotted versus d.c. bias current $I$ and gate voltage $V_G$ on a well-quantized $\nu = 2$ plateau at $B = 3$ T. Gate-dependent oscillations centred at zero bias are observed, indicating interference of the CAESs. **b**–**d**, Bias-dependent oscillations of $\tilde{R}_{xx}$ at gate voltages $V_G = 5.08$ (**b**), 5.19 (**c**) and 5.29 V (**d**) (see arrows in **a**). Oscillations die out with increasing temperature. **e**, The dispersion relation of a pair of CAESs at a quantum Hall–superconductor interface calculated from the tight-binding simulation. The momentum difference between the two modes varies with energy, causing oscillations of $\tilde{R}_{xx}$ in bias.

Figure 1d shows the results of our simulation describing an electron injected in a quantum Hall edge state towards an interface with a superconductor. Note the clear beating pattern between the electron and hole probabilities. The value of the chemical potential was chosen such that the outgoing state was almost purely a hole. We can alternatively obtain an outgoing electron, or any superposition of electron and hole, by changing the chemical potential in our simulation, which corresponds to varying the gate voltage in the experiment. As a result, the calculated probabilities of the outgoing state being an electron ($P_e$) or a hole ($P_h$) show pronounced oscillations (Supplementary Fig. 12).

Experimentally, the beating pattern between the two CAESs is likely to be affected by multiple parameters, such as the interface roughness, disorder potential, electron density profile near the contact and even positions of vortices in the superconducting contact (Supplementary Figs. 5 and 6). As a result, the downstream resistance measured as a function of the gate voltage acquires a pattern of random but highly reproducible fluctuations (Fig. 1c), in which the signal is positive or negative depending on whether the superconductor emits predominantly an electron or a hole. We next provide further experimental evidence that supports our interpretation of the non-zero downstream resistance.

## Dependence of $\tilde{R}_{xx}$ on magnetic field

The behaviour observed in Fig. 1c is generic. In Fig. 2a, we plot $\tilde{R}_{xx}$ and $G_{xy}$ at 3 T for a wider range of gate voltages. Clearly, $\tilde{R}_{xx}$ oscillates around zero as a function of the gate voltage for a range of integer filling factors. We could also expect mesoscopic fluctuations in the downstream resistance to be induced by changing the magnetic field, $B$, which changes the magnetic length. Indeed, our simulations indicate that $P_e - P_h$ oscillates with the magnetic field (Supplementary Fig. 13).

To explore this dependence experimentally, we plot $\tilde{R}_{xx}$ as a function of both $B$ and $V_G$ in Fig. 2b. The overall pattern is reminiscent of the traditional Landau fan diagram of longitudinal resistance, with the exception that the downstream resistance $\tilde{R}_{xx}$ is not equal to zero on the plateaux. Mesoscopic fluctuations that deviate from zero resistance (white) appear inside the quantum Hall plateaux as blue (negative) and red (positive) pockets. A prominent feature of the data is the frequent abrupt changes of the $\tilde{R}_{xx}(V_G)$ pattern while sweeping the magnetic field. Although the field sweeps are stable and reproducible in a very small range of $B$, changing the field by several mT completely changes the curves (see Supplementary Fig. 5b for more details). This stochastic switching complicates analysis of the map.

We note that when switching of the $\tilde{R}_{xx}(V_G)$ curve occurs, $G_{xy}$ stays unchanged (compare Figs. 1b and 2b). This can also be noticed in Supplementary Fig. 5a in the regions slightly outside the quantized plateau, where $G_{xy}$ develops a recognizable mesoscopic pattern. This observation indicates that the switching events do not involve the normal contacts 'b' and 'd' between which $G_{xy}$ is measured, nor the bulk of the sample. Instead, they must originate in the superconducting contact 'c'. We surmise that switching of the $\tilde{R}_{xx}$ pattern is caused by the rearrangement of vortices inside the type II superconducting contact. Indeed, we have routinely observed similar switching events in the interference pattern of supercurrent in Josephson junctions fabricated with similar contacts. In Supplementary Section 4, we show that we can hysteretically switch between two distinct patterns of $\tilde{R}_{xx}$ multiple times, indicating that the vortices can be controllably added to and removed from the superconductor.

To explain the observed sensitivity of $\tilde{R}_{xx}$ to the vortex configuration, we note that adding a vortex close to the interface should change the phase of the order parameter along the quantum Hall–superconductor interface, $\theta(x)$. As a result of this change, a pure electron or pure hole state would only acquire an overall phase, which would not change $\tilde{R}_{xx}$. However, the change of $\theta(x)$ is expected to change the relative phase shift between the two interfering CAESs. The presence of the vortices is typically neglected in theoretical studies, but we find that they have a dramatic effect on the beating pattern of the CAESs—in Supplementary Fig. 12 we show that the $P_e$-$P_h$ curve is completely scrambled by adding just a single vortex, modeled as a kink in $\theta(x)$.

To extract information otherwise buried in the stochastic switching, we analyse the impact of $B$ on the gate-dependent oscillations on the $\nu = 2$ plateau (more statistical analysis can be found in

Supplementary Section 7). The plateau region used for this analysis is selected such that $G_{xy}$ is within 1% off the quantized values, as indicated by the black lines in Fig. 2b. We then find the minimum and maximum $\tilde{R}_{xx}(V_{\mathrm{G}})$ for a given field and plot the resulting $\min\tilde{R}_{xx}(V_{\mathrm{G}})$ and $\max\tilde{R}_{xx}(V_{\mathrm{G}})$ as a function of $B$ in Fig. 2c. First, we find that the amplitude of the fluctuations decreases with $B$. This suppression is most probably explained by the CAESs being absorbed by the contact, thereby creating quasiparticle excitations in the superconductor. (These excitations are possibly absorbed by the normal cores of the vortices.) Evidently, this process becomes more effective at higher $B$. Second, the typical amplitudes of the positive and negative signals are very close. We argue that this observation indicates that CAESs are, on average, neutral (Supplementary Sections 2 and 6). Indeed, if the two CAESs $\psi_{1,2}$ had predominantly electron-like and hole-like characters, respectively, the incoming electron would couple primarily to state $\psi_1$. This would, in turn, result in a greater likelihood of electrons being emitted downstream, and $\tilde{R}_{xx}$ would mostly stay positive, that is, $\max\tilde{R}_{xx}(V_{\mathrm{G}}) > |\min\tilde{R}_{xx}(V_{\mathrm{G}})|$, contrary to our observations.

Our numerical simulations support this argument: the eigenmodes $\psi_{1,2}$ are given by coherent superpositions of electron and hole amplitudes, which have distinct patterns in space. Nevertheless, the integral of the probability of the electron and hole components is close to 1/2 (Supplementary Fig. 11), resulting in the overall approximately neutral character of the CAES. Due to particle–hole symmetry of the model, $\psi_2$ at zero energy is the charge conjugate partner of $\psi_1$, meaning that the pattern of the electron and hole amplitudes is interchanged.

## Dispersion of CAESs

Finally, we address the nonlinearity of the CAES energy–momentum dispersion. In Fig. 3a, we plot the $\tilde{R}_{xx}$ map measured as a function of $I$ and $V_{\mathrm{G}}$. The data correspond to the range nominally identical to Fig. 1c, but it was measured following a sweep of magnetic field, so the individual mesoscopic features have changed. The dependence of this map on temperature and additional maps for $\nu = 6$ are provided in Supplementary Section 5.

Most notably, we find that $\tilde{R}_{xx}$ in Fig. 3a oscillates not only with the gate voltage, but also as a function of the d.c. current bias. These oscillations are revealed in the vertical cross-sections of the map, taken at $V_{\mathrm{G}} = 5.08$, 5.19 and 5.29 V and plotted in Fig. 3b–d. Quite unusually, the signal can even oscillate several times as a function of bias, as shown in Fig. 3c. To interpret these oscillations, we note that the applied current tunes the energy of the injected electrons with respect to the grounded superconducting contact, $E = eI/G_{xy}$. The wavevector difference $\delta k$ between the two CAESs depends on their energy, as demonstrated in our model calculations in Fig. 3e (Supplementary Section 6). The phase difference accumulated by the CAESs along the interface, $\delta kL$, thus produces the observed bias oscillations of $\tilde{R}_{xx}$. Eventually, $\tilde{R}_{xx}$ goes to zero when the applied voltage becomes comparable to the superconducting gap, $I/G_{xy} \approx \Delta/e$. At that point, the incoming electrons have high probability to enter the superconductor as quasiparticles, and no downstream signal is expected.

## Outlook

We have demonstrated robust coupling of the quantum Hall edge states to a superconductor via Andreev reflections, resulting in the formation of chiral Andreev edge states—coherent superpositions of electrons and holes. Further study of CAESs may focus on increasing the strength of the downstream signal and making the oscillation pattern more regular, both of which could be achieved by shortening the superconducting interface and reducing the magnetic field. Such developments could in turn lead to realization of novel quantum effects and devices, possible examples being Bogoliubov quasiparticle annihilation[36], a superconducting flux capacitor[37] and a phase-coherent heat circulator[38]. Finally, the non-local downstream voltage measurement implemented here could also be applied to samples in which the quantum Hall effect is replaced by the quantum anomalous Hall effect. In this case, the neutral interfacial modes are predicted to be chiral Majorana fermions[30].

## Online content

Any methods, additional references, Nature Research reporting summaries, source data, extended data, supplementary information, acknowledgements, peer review information; details of author contributions and competing interests; and statements of data and code availability are available at https://doi.org/10.1038/s41567-020-0898-5.

Received: 29 July 2019; Accepted: 7 April 2020;

## References

1. Klapwijk, T. M. Proximity effect from an Andreev perspective. *J. Supercond.* **17**, 593–611 (2004).
2. Beenakker, C. W. J. Random-matrix theory of Majorana fermions and topological superconductors. *Rev. Mod. Phys.* **87**, 1037–1066 (2015).
3. Stern, A. & Lindner, N. H. Topological quantum computation—from basic concepts to first experiments. *Science* **339**, 1179–1184 (2013).
4. Lian, B., Sun, X.-Q., Vaezi, A., Qi, X.-L. & Zhang, S.-C. Topological quantum computation based on chiral Majorana fermions. *Proc. Natl Acad. Sci. USA* **115**, 10938–10942 (2018).
5. Lutchyn, R. M. et al. Majorana zero modes in superconductor–semiconductor heterostructures. *Nat. Rev. Mater.* **3**, 52–68 (2018).
6. Mong, R. S. K. et al. Universal topological quantum computation from a superconductor-Abelian quantum Hall heterostructure. *Phys. Rev. X* **4**, 011036 (2014).
7. Qi, X.-L., Hughes, T. L. & Zhang, S.-C. Chiral topological superconductor from the quantum Hall state. *Phys. Rev. B* **82**, 184516 (2010).
8. Takagaki, Y. Transport properties of semiconductor–superconductor junctions in quantizing magnetic fields. *Phys. Rev. B* **57**, 4009–4016 (1998).
9. Hoppe, H., Zülicke, U. & Schön, G. Andreev reflection in strong magnetic fields. *Phys. Rev. Lett.* **84**, 1804–1807 (2000).
10. Khaymovich, I. M., Chtchelkatchev, N. M., Shereshevskii, I. A. & Mel'nikov, A. S. Andreev transport in two-dimensional normal-superconducting systems in strong magnetic fields. *Europhys. Lett.* **91**, 17005 (2010).
11. Chamon, C., Jackiw, R., Nishida, Y., Pi, S.-Y. & Santos, L. Quantizing Majorana fermions in a superconductor. *Phys. Rev. B* **81**, 224515 (2010).
12. Tiwari, R. P., Zülicke, U. & Bruder, C. Majorana fermions from Landau quantization in a superconductor and topological-insulator hybrid structure. *Phys. Rev. Lett.* **110**, 186805 (2013).
13. Gamayun, O., Hutasoit, J. A. & Cheianov, V. V. Two-terminal transport along a proximity-induced superconducting quantum Hall edge. *Phys. Rev. B* **96**, 241104 (2017).
14. Chaudhary, G. & MacDonald, A. H. Vortex-lattice structure and topological superconductivity in the quantum Hall regime. *Phys. Rev. B* **101**, 024516 (2020).
15. Eroms, J., Weiss, D., Boeck, J. D., Borghs, G. & Zülicke, U. Andreev reflection at high magnetic fields: evidence for electron and hole transport in edge states. *Phys. Rev. Lett.* **95**, 107001 (2005).
16. Batov, I. E., Schäpers, T., Chtchelkatchev, N. M., Hardtdegen, H. & Ustinov, A. V. Andreev reflection and strongly enhanced magnetoresistance oscillations in $\mathrm{Ga}_x\mathrm{In}_{1-x}\mathrm{As}$/InP heterostructures with superconducting contacts. *Phys. Rev. B* **76**, 115313 (2007).
17. Komatsu, K., Li, C., Autier-Laurent, S., Bouchiat, H. & Guéron, S. Superconducting proximity effect in long superconductor/graphene/superconductor junctions: from specular Andreev reflection at zero field to the quantum Hall regime. *Phys. Rev. B* **86**, 115412 (2012).
18. Rickhaus, P., Weiss, M., Marot, L. & Schönenberger, C. Quantum Hall effect in graphene with superconducting electrodes. *Nano Lett.* **12**, 1942–1945 (2012).
19. Wan, Z. et al. Induced superconductivity in high-mobility two-dimensional electron gas in gallium arsenide heterostructures. *Nat. Commun.* **6**, 7426 (2015).
20. Ben Shalom, M. et al. Quantum oscillations of the critical current and high-field superconducting proximity in ballistic graphene. *Nat. Phys.* **12**, 318–322 (2016).
21. Calado, V. E. et al. Ballistic Josephson junctions in edge-contacted graphene. *Nat. Nanotechnol.* **10**, 761–764 (2015).
22. Amet, F. et al. Supercurrent in the quantum Hall regime. *Science* **352**, 966–969 (2016).
23. Seredinski, A. et al. Quantum Hall-based superconducting interference device. *Sci. Adv.* **5**, eaaw8693 (2019).
24. Lee, G.-H. et al. Inducing superconducting correlation in quantum Hall edge states. *Nat. Phys.* **13**, 693–698 (2017).

25. Sahu, M. R. et al. Inter-Landau-level Andreev reflection at the Dirac point in a graphene quantum Hall state coupled to a $NbSe_2$ superconductor. *Phys. Rev. Lett.* **121**, 086809 (2018).
26. Park, G.-H., Kim, M., Watanabe, K., Taniguchi, T. & Lee, H.-J. Propagation of superconducting coherence via chiral quantum-Hall edge channels. *Sci. Rep.* **7**, 10953 (2017).
27. Kozuka, Y., Sakaguchi, A., Falson, J., Tsukazaki, A. & Kawasaki, M. Andreev reflection at the interface with an oxide in the quantum Hall regime. *J. Phys. Soc. Jpn* **87**, 124712 (2018).
28. Matsuo, S. et al. Equal-spin Andreev reflection on junctions of spin-resolved quantum Hall bulk state and spin-singlet superconductor. *Sci. Rep.* **8**, 3454 (2018).
29. van Ostaay, J. A. M., Akhmerov, A. R. & Beenakker, C. W. J. Spin-triplet supercurrent carried by quantum Hall edge states through a Josephson junction. *Phys. Rev. B* **83**, 195441 (2011).
30. Lian, B., Wang, J. & Zhang, S.-C. Edge-state-induced Andreev oscillation in quantum anomalous Hall insulator–superconductor junctions. *Phys. Rev. B* **93**, 161401 (2016).
31. Wang, L. et al. One-dimensional electrical contact to a two-dimensional material. *Science* **342**, 614–617 (2013).
32. Borzenets, I. V. et al. Ballistic graphene Josephson junctions from the short to the long junction regimes. *Phys. Rev. Lett.* **117**, 237002 (2016).
33. Roulleau, P. et al. Direct measurement of the coherence length of edge states in the integer quantum Hall regime. *Phys. Rev. Lett.* **100**, 126802 (2008).
34. Petković, I. et al. Carrier drift velocity and edge magnetoplasmons in graphene. *Phys. Rev. Lett.* **110**, 016801 (2013).
35. Akhmerov, A. R. & Beenakker, C. W. J. Detection of valley polarization in graphene by a superconducting contact. *Phys. Rev. Lett.* **98**, 157003 (2007).
36. Beenakker, C. W. J. Annihilation of colliding Bogoliubov quasiparticles reveals their Majorana nature. *Phys. Rev. Lett.* **112**, 070604 (2014).
37. Clarke, D. J., Alicea, J. & Shtengel, K. Exotic circuit elements from zero-modes in hybrid superconductor–quantum-Hall systems. *Nat. Phys.* **10**, 877–882 (2014).
38. Hwang, S.-Y., Giazotto, F. & Sothmann, B. Phase-coherent heat circulator based on multiterminal Josephson junctions. *Phys. Rev. Appl.* **10**, 044062 (2018).

## Methods

**Device fabrication.** The heterostructure was assembled from separately exfoliated flakes of graphene and hBN. These flakes were deposited onto a diced silicon wafer capped with a 280 nm thermally grown oxide layer. The substrate was baked to remove moisture (200 °C for 10 min) and oxygen plasma ashed (10 s at 500 mbar) in the case of hBN.

The flakes were assembled with the dry transfer technique and picked up with a polydimethylsiloxane (PDMS)/polycarbonate (PC) stamp. For the latter, a 2 × 2 mm square of PDMS was first cut and attached to a glass slide with transparent, double-sided tape. Meanwhile, PC film (6 g suspended per 100 ml chloroform) was prepared by drop-coating a separate slide and levelling the layer by dragging another clean slide across it, before leaving the solvent to evaporate. The PC layer was then picked up with double-sided tape and placed (tape side down) over the PDMS square. The resulting PDMS/PC stamp was then cured for 5 min at 110 °C.

Individual flakes were picked up with the stamp at 70 °C and then deposited onto a clean Si/SiO$_2$ substrate at 150 °C. The finished stack was cleaned of stamp residue in hot dichloromethane for 10 min followed by a 30 min anneal step at 500 °C in atmosphere. This had the additional benefit of consolidating the 'bubbles' of trapped hydrocarbons within the heterostructure, leaving larger defect-free regions. A clean region of encapsulated graphene to be used for the device was identified using atomic force microscopy and Raman spectroscopy mapping.

Patterning of the heterostructure was achieved by electron-beam lithography on a layer of PMMA resist. We used SF$_6$ to etch the top layer of hBN, followed by CHF$_3$/O$_2$ to etch the graphene layer. The electrodes were deposited immediately after etching the contact region to ensure a fresh graphene–metal interface. The normal metal electrodes were made of thermally evaporated Cr (1 nm)/Au (100 nm). The superconducting electrodes comprised 100 nm MoRe alloy (50–50 ratio by weight) d.c. sputtered in a high-vacuum chamber ($10^{-8}$ torr).

**Measurements.** Measurements were performed in a Leiden Cryogenics dilution refrigerator at a temperature of 100 mK unless otherwise stated. The sample was held in the refrigerator by resistive coax lines and low-temperature *RC* filters. Differential resistance measurements were carried out using a 10 nA square-wave excitation with home-made preamplifiers and a NI-6363 data acquisition board. The excitation frequency was chosen to be 15 Hz to maximize 60 Hz noise reduction. The response to the square-wave step was allowed to settle for a time greater than the *RC* time of the filters before recording the voltage.

## Data availability

Source data for figures (including the supplementary figures) are available in the public repository Zenodo (https://doi.org/10.5281/zenodo.3708374)[39]. All other data that support the plots within this paper and other findings of this study are available from the corresponding author upon reasonable request.

## Code availability

The codes used for the analysis and simulations are available in the public repository Zenodo (https://doi.org/10.5281/zenodo.3708374)[39].

## References

39. Zhao, L. et al. *Data and Codes for 'Interference of Chiral Andreev Edge States'* (Zenodo, 2020); https://doi.org/10.5281/zenodo.3708374

## Acknowledgements

We greatly appreciate stimulating discussion with A. Chang, M. Gilbert, B. Lian, Y. Oreg, K. Shtengel and A. Stern. Transport measurements conducted by L.Z., E.G.A. and A.S. were supported by the Division of Materials Sciences and Engineering, Office of Basic Energy Sciences, US Department of Energy, under award no. DE-SC0002765. Lithographic fabrication and characterization of the samples was performed by L.Z. and A.S. with the support of NSF awards ECCS-1610213 and DMR-1743907. The measurement set-up was developed by A.W.D., T.F.Q.L. and G.F. with the support of ARO award W911NF-16-1-0122. Numerical simulations conducted by A.B. and H.U.B. were supported by the Division of Materials Sciences and Engineering, Office of Basic Energy Sciences, US Department of Energy, under award no. DE-SC0005237. H.L. and F.A. acknowledge support from ARO (award W911NF-16-1-0132). K.W. and T.T. acknowledge support from JSPS KAKENHI grant no. JP15K21722 and the Elemental Strategy Initiative conducted by the MEXT, Japan. T.T. acknowledges support from JSPS Grant-in-Aid for Scientific Research A (no. 26248061) and JSPS Innovative Areas Nano Informatics (no. 25106006). Sample fabrication was performed in part at the Duke University Shared Materials Instrumentation Facility (SMIF), a member of the North Carolina Research Triangle Nanotechnology Network (RTNN), which is supported by the National Science Foundation (grant no. ECCS-1542015) as part of the National Nanotechnology Coordinated Infrastructure (NNCI).

## Author contributions

L.Z. and A.S. characterized and fabricated the device. H.L. and F.A. made the graphene–hBN heterostructure. T.T. and K.W. provided the hBN crystals. L.Z., E.G.A. and A.S. performed the measurements. A.W.D., T.F.Q.L. and G.F. developed the measurement set-up. A.B. and H.U.B. conducted the numerical calculations. L.Z. and G.F. analysed the data and wrote the manuscript. H.U.B., F.A. and G.F. supervised the project.

## Competing interests

The authors declare no competing interests.

## Additional information

**Supplementary information** is available for this paper at https://doi.org/10.1038/s41567-020-0898-5.

**Correspondence and requests for materials** should be addressed to L.Z. or G.F.

**Peer review information** *Nature Physics* thanks Leonid Rokhinson and the other, anonymous, reviewer(s) for their contribution to the peer review of this work.

**Reprints and permissions information** is available at www.nature.com/reprints.